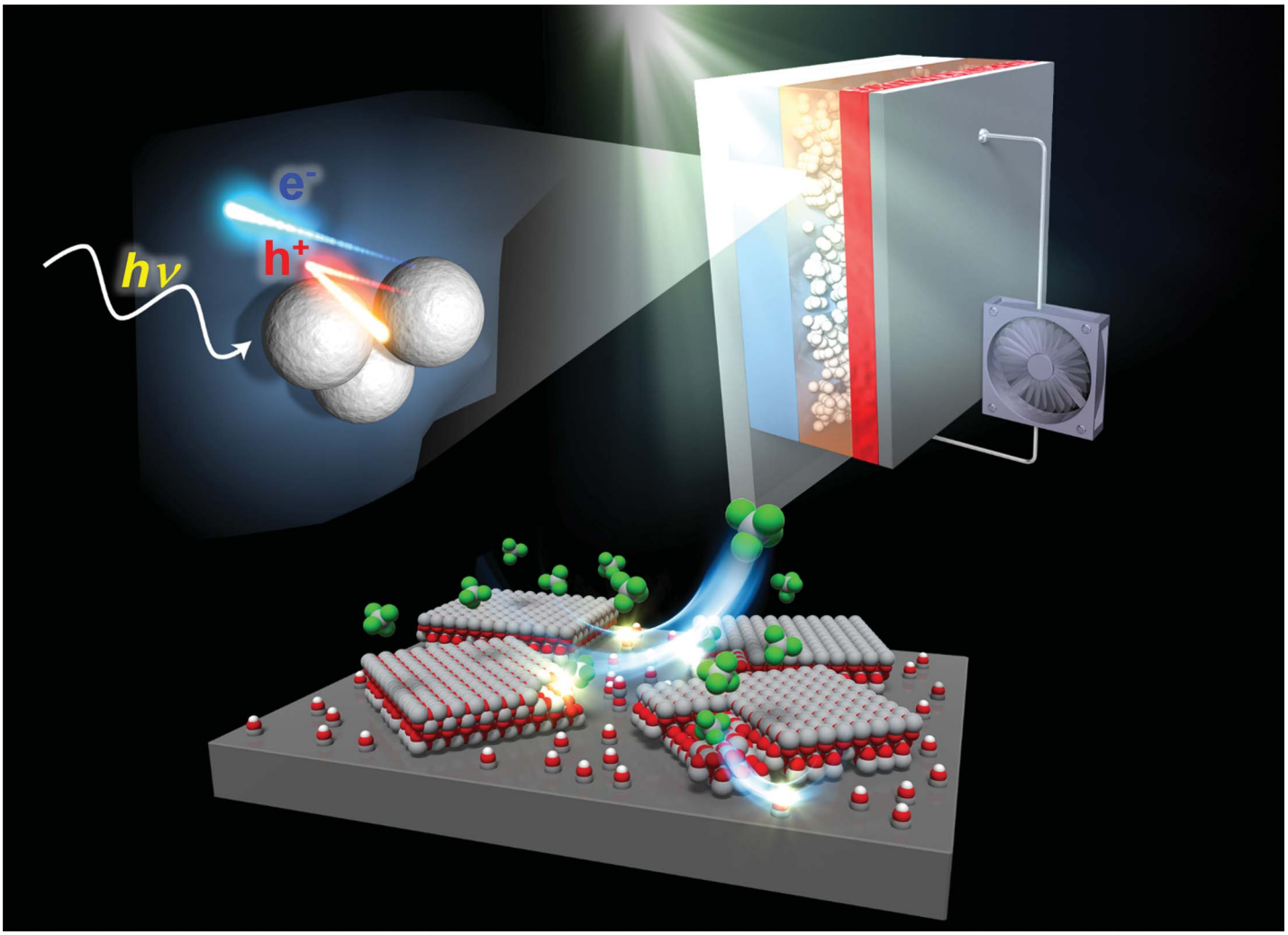

Showcasing research from Prof. Hiroaki Misawa's group at Hokkaido University, Japan and National Chiao Tung University, Taiwan, and Prof. Eric Diau's group at National Chiao Tung University, Taiwan.

Optimization of a compact layer of TiO_2 *via* atomic-layer deposition for high-performance perovskite solar cells

A uniform and pinhole-free compact layer of TiO_2 was produced *via* atomic-layer deposition for mesoporous perovskite solar cells with a n-i-p configuration. The best power conversion efficiency of the cell attained 15.0% with a minor hysteresis effect. The devices showed great stability and reproducibility, providing an alternative for high-performance perovskite solar cells.

As featured in:

See Eric Wei-Guang Diau, Hiroaki Misawa *et al.*, *Sustainable Energy Fuels*, 2017, **1**, 1533.

ROYAL SOCIETY OF CHEMISTRY

rsc.li/sustainable-energy

Registered charity number: 207890

Sustainable Energy & Fuels

PAPER

View Article Online
View Journal | View Issue

Cite this: *Sustainable Energy Fuels*, 2017, **1**, 1533

Optimization of a compact layer of TiO_2 *via* atomic-layer deposition for high-performance perovskite solar cells†

Ahmed Esmail Shalan,[a] Sudhakar Narra,[b] Tomoya Oshikiri,[a] Kosei Ueno,[a] Xu Shi,[a] Hui-Ping Wu,[b] Mahmoud M. Elshanawany,[b] Eric Wei-Guang Diau*[b] and Hiroaki Misawa*[ab]

We report the effect of thickness of a film consisting of a compact layer of TiO_2 produced *via* atomic-layer deposition (ALD) for mesoporous perovskite solar cells (PSCs) with a n-i-p configuration. Uniform and pinhole-free TiO_2 films of thickness from 10 to 400 nm were deposited on fluorine-doped tin-oxide substrates using ALD. The device performance of the PSC showed a trend systematic with the thickness of the ALD-TiO_2 compact layer and attained the best efficiency, 15.0%, of power conversion at thickness 200 nm. Photoluminescence (PL) spectra and the corresponding PL decays for perovskite (PSK) deposited on varied ALD-TiO_2 films were recorded; the effective PL quenching is due to electron transfer from PSK into the ALD-TiO_2 compact layer. The most efficient interfacial electron transfer occurred at film thickness 200 nm, for which the ALD-TiO_2 film has the greatest surface roughness and conductivity. We found a systematic correlation between the device performance in relation to the conductivity and the rate of interfacial electron transfer as a function of thickness of the ALD-TiO_2 film; the best performance occurred at thickness 200 nm. The devices showed great stability and reproducibility, providing an alternative for high-performance PSCs with a well-controlled TiO_2 compact layer.

Received 25th April 2017
Accepted 20th June 2017

DOI: 10.1039/c7se00220c

rsc.li/sustainable-energy

Introduction

In 2009, Miyasaka and co-workers employed $CH_3NH_3PbI_3$ (also called perovskite (PSK) or $MAPbI_3$) as the light absorber in solar cells and achieved power conversion efficiency (PCE) of 3.8%.[1] Miyasaka's and Snaith's groups improved the structure of the perovskite solar cells (PSCs) to attain a PCE approaching 10%.[2] As a result, much attention was paid to the development of PSCs. Seok's group has obtained a certified PCE of 20.1% (ref. 3) for PSCs. The advantages of high efficiency and low cost of production make PSCs competitive with conventional silicon-based solar cells.[4,5]

The photo-generated charge carriers (both electrons and holes) in PSCs are formed in the organo-metal halide PSK layer, which can also transport carriers with diffusion lengths exceeding 1 μm.[6] The compact layer (or hole-blocking layer (HBL) in a n-i-p device) is able to extract and to collect photo-generated electrons and can also prevent holes formed in the PSK from reaching the fluorine-doped tin-oxide (FTO) electrode. A TiO_2 film in a compact layer of several nanometers thickness served to inhibit electron–hole recombination and to avoid direct contact between the PSK layer and the FTO electrode.[7]

As a hysteresis effect is a central problem in PSCs, much effort has been devoted to understand the cause of hysteresis; for instance, ferroelectricity,[8–10] ion mobility[11–13] and defects[14,15] of PSK in addition to device structure[16,17] have been proposed, but the relationship between the compact layer and the hysteresis effect is less understood.

Various conventional methods including spin coating,[18] spray pyrolysis,[19,20] electrochemical deposition[21] and thermal oxidation[22,23] were used to prepare a TiO_2 compact layer. With these methods, thermal post-treatments at high temperature (>450 °C) are required to ensure adequate electronic contact. Such a treatment not only greatly increases the cost of fabrication and presents drawbacks in view of industrial-scale roll to roll fabrication[24] due to a lack of compatibility with flexible substrates, but also increases the occurrence of pinholes in the TiO_2 compact film,[25] which impair the performance of PSCs.[26] In addition, these methods generally make a precise control of the thickness of a compact layer film more challenging.

Compared with conventional techniques for the preparation of the compact layer, atomic-layer deposition (ALD) has additional advantages of operating at a low temperature, offering

[a]*Research Institute for Electronic Science, Hokkaido University, N21, W10, Kita-ku, 001-0021, Sapporo, Japan. E-mail: misawa@es.hokudai.ac.jp*

[b]*Department of Applied Chemistry, National Chiao Tung University, 1001 Ta Hsueh Road, Hsinchu 30010, Taiwan. E-mail: diau@mail.nctu.edu.tw*

† Electronic supplementary information (ESI) available. See DOI: 10.1039/c7se00220c

a precise control of thickness and yielding excellent conformity and uniformity of the film.[27–29] ALD is hence capable of depositing a homogeneous pinhole-free film of TiO_2 on the photoanode of a PSC as it involves the chemical reactions of volatile, metal and oxidizing precursors at two separate stages in which no sintering is required after the deposition of the HBL. This phenomenon can be confirmed with photoluminescence (PL) spectra and the corresponding PL decays for PSK deposited on varied ALD-TiO_2 films. Although there are several reports regarding PSCs with ALD-TiO_2 compact layers,[30–32] a systematic study of the device performance and hysteresis of PSCs with a wide range of thickness of ALD-TiO_2 film has not been reported.

In this work, we deposited TiO_2 compact layers of film thickness varied from 10 to 400 nm onto a FTO-coated glass substrate by ALD. We prepared a mesoporous PSC according to a typical n-i-p device configuration, and characterized the corresponding photovoltaic performance and the hysteresis effect. The device performance was correlated with the PL intensity and the rate of electron transfer that is characterized with time-correlated single-photon-counting (TCSPC).

Results and discussion

Fig. 1 presents a schematic structure and energy diagram for a PSC employing a compact ALD-TiO_2 film as HBL and spiro-OMeTAD as the hole-transfer layer (HTL). The TiO_2 HBL plays an important role in the planar structured devices for both electron extraction at the TiO_2/PSK interface and electron transfer through itself, in addition to avoiding direct contact between PSK and FTO. Such planar devices commonly exhibit small efficiency because of the decreased ability of charge transport and extraction and increased charge recombination.[33] TiO_2 has slower electron migration ability[34,35] than PSK and hole-transfer materials; the thickness of the compact layer is likely to affect the electron transport. To separate the influences from the electron extraction and transport processes, we fabricated mesoporous structured devices with the HBL using the ALD-TiO_2 films. This approach can also avert the impact of various morphologies of compact layers on the crystallization of PSK. Fig. 1a presents the configuration of the PSC in this work. The TiO_2 compact layer was first deposited on FTO glass by ALD, followed by addition of a mesoporous TiO_2 layer *via* screen printing; a $CH_3NH_3PbI_3$ light harvester was then deposited through an anti-solvent process.[36] The details of the experimental methods are described in the experimental section and the fabrication step by step is shown in Fig. S1.† After that, an organic HTL spiro-OMeTAD and a silver contact electrode were consecutively patterned and deposited on top of the PSK layer to complete the fabrication of the solar cell with the structure of glass/FTO/compact ALD-TiO_2/m-TiO_2/$MAPbI_3$/spiro-OMeTAD/Ag. Fig. 1b illustrates the possible transport of photo-generated carriers and presents a potential-energy diagram of each layer in the cell. A satisfactory match of band energies enables the electron–hole separation to occur easily in the PSK layer.

To confirm the structure of the cells layer by layer and the thicknesses of the prepared ALD-TiO_2 films, we characterized the cross-sections using a field-emission scanning electron microscope (FESEM). Fig. 2a–f present images of the cross-section of a full PSC using ALD-TiO_2 as HBL with thickness 10, 50, 100, 200, 300 and 400 nm, respectively. The thickness of the whole PSK layer is controlled to about 330 nm with a ~230 nm thick layer of mesoporous TiO_2 (m-TiO_2) and a PSK layer of thickness ~100 nm. On top of the PSK layer, we deposited an organic HTL (spiro-OMeTAD) followed by a silver contact electrode of thickness ~150 nm. All images show a satisfactory contact between each layer that facilitates the charge migration in their paths, which improves the PCE of the cells as the results show below. Both the compact TiO_2 and the mesoporous layers play an important role in the extraction of the interfacial charge because of the large surface area and the influence of the satisfactory morphology which facilitate efficient charge extraction and prevent direct contact of the hole with the FTO substrate.

Fig. 3a and b show the *J–V* characteristics and the corresponding spectra of the efficiency of conversion of incident photons to current (IPCE), respectively. The improved PCE in Fig. 3a is attributed to the increased short-circuit current (J_{sc}) and fill factor (FF) for the effective extraction of interfacial charge with the thickness of the ALD-TiO_2 layer varied from 10 nm to 200 nm. When the ALD-TiO_2 film was thicker than 200 nm, the decreased conductivity in those ALD-TiO_2 devices deteriorated the performance, as revealed by decreased J_{sc} and FF for the devices with ALD-TiO_2 of thicknesses 300 and 400 nm

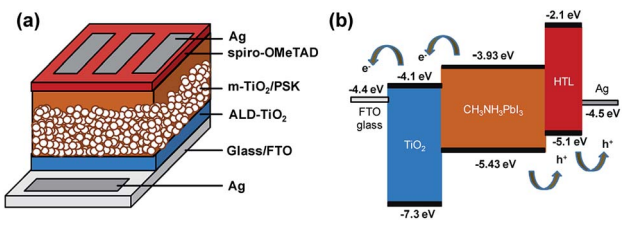

Fig. 1 (a) Configuration of the PSC: glass/FTO/ALD-TiO_2/m-TiO_2/$MAPbI_3$/spiro-OMeTAD/Ag. (b) Diagram of energy levels of each layer of the PSC.

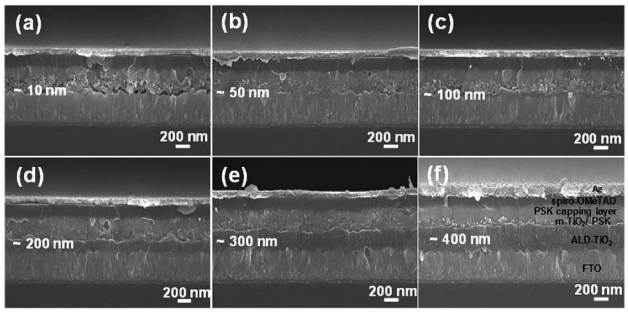

Fig. 2 Cross-section SEM of the PSCs with ALD-TiO_2 as HBL of thickness (a) 10, (b) 50, (c) 100, (d) 200, (e) 300 and (f) 400 nm. The magnification is ×20 000; the scale bar is 200 nm for all SEM images.

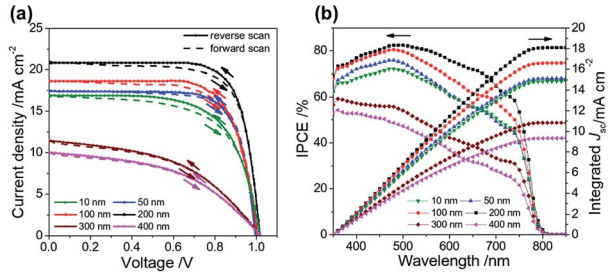

Fig. 3 (a) *J–V* curves, (b) IPCE and integrated current density of ALD-TiO_2 with thickness 10, 50, 100, 200, 300 and 400 nm, respectively, as a compact HBL for the best PSC.

as discussed below. The open-circuit voltages (V_{oc}) of all ALD-TiO_2 devices appeared to be nearly constant, which confirms that a variation of the film thickness produces no leakage of electrons and holes. The ALD-TiO_2 devices exhibit only a small effect of hysteresis for all thicknesses of the ALD-TiO_2 compact layer (Fig. 3a). The scan range with varied initial bias plays an important role in the hysteretic behavior and can alter the PV performance.[8] A forward scan with a negative starting bias would deteriorate the efficiency, whereas a reverse scan starting with a positive applied bias would increase the performance.[37] For each device, the lack of noticeable difference in J_{sc} observed in Fig. 3a is due to the fact that a given voltage-settling interval is too short to distinguish the small difference in capacitive current.[38,39] The PSK film is thin in this work; a thicker PSK layer generally has more defects, which might cause a more serious charge accumulation and a more explicit hysteresis effect. Table 1 summarizes the photovoltaic parameters J_{sc}, V_{oc}, FF and PCE of the ALD-TiO_2-based PSC devices.

According to the IPCE spectra in Fig. 3b, the best device showed an excellent photocurrent response from 400 to 800 nm, with a maximum IPCE of ~80%. Fig. 3b also shows that integrating the IPCE over the AM1.5 solar spectrum at irradiance 100 mW cm^{-2} gives J_{sc} estimated to be 14.8, 15.1, 16.6, 18.1, 10.8 and 9.3 mA cm^{-2} for ALD-TiO_2 devices of thickness 10, 50, 100, 200, 300 and 400 nm, respectively. Under the solar simulator for these cells, J_{sc} was measured to be 16.9, 17.4, 18.6, 20.8, 11.5 and 10.1 mA cm^{-2}, respectively. The differences between the current estimated from the IPCE integration and the *J–V* measurements are within the experimental uncertainties. We also note that we tested these cells in air without encapsulation: there is typically a slightly degraded performance for these PSCs following testing.[40]

To understand the influence of TiO_2 HBL coverage on the device performance, we studied the morphologies of the samples with an atomic-force microscope (AFM). The surface topographies of the ALD-TiO_2 compact layer of thickness 10, 50, 100, 200, 300 and 400 nm on FTO so determined are shown in Fig. 4a–g. The root-mean-square roughness (R_{rms}) of bare FTO was 11.8 nm; R_{rms} was 16.3, 20.4, 29.6, 33.9, 25.1, and 22.4 nm for ALD-TiO_2 thickness 10, 50, 100, 200, 300, and 400 nm, respectively. The surface roughness of every ALD-TiO_2 film was thus slightly more rugged than that of the bare FTO substrate and increased with the thickness of the TiO_2 film until 200 nm before decreasing again for 300 and 400 nm. The top-view images of FESEM of the TiO_2 film also indicate that the grain size of TiO_2 reaches the maximum when the TiO_2 film thickness is 200 nm (Fig. S2†). This phenomenon can be explained in what follows. At first, nucleation of crystals occurred on the

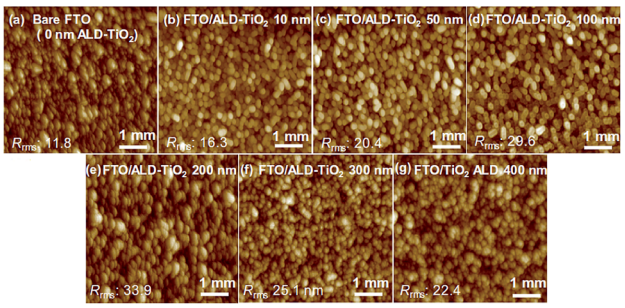

Fig. 4 AFM of (a) bare FTO, (b) FTO/ALD-TiO_2 10 nm, (c) FTO/ALD-TiO_2 50 nm, (d) FTO/ALD-TiO_2 100 nm, (e) FTO/ALD-TiO_2 200 nm, (f) FTO/ALD-TiO_2 300 nm, (g) FTO/ALD-TiO_2 400 nm. The magnification is ×12 500; the scale bar is 1 μm for all AFM images.

Table 1 Photovoltaic parameters (reverse and forward scan) of a PSC fabricated with compact ALD-TiO_2 HBL of varied thickness

Devices with ALD-TiO_2[a]		J_{sc}/mA cm^{-2}	V_{oc}/V	FF	PCE[b]/%
10 nm	Reverse scan	16.90	1.00	0.565	9.55 (9.33 ± 0.14)
	Forward scan	16.74	1.02	0.557	9.51
50 nm	Reverse scan	17.44	1.00	0.599	10.45 (9.76 ± 0.33)
	Forward scan	17.57	1.00	0.618	10.85
100 nm	Reverse scan	18.63	1.01	0.689	12.97 (12.78 ± 0.19)
	Forward scan	18.96	1.02	0.685	13.25
200 nm	Reverse scan	20.81	1.03	0.702	15.03 (14.37 ± 0.44)
	Forward scan	21.00	1.02	0.719	15.41
300 nm	Reverse scan	11.46	1.03	0.693	8.18 (7.68 ± 0.23)
	Forward scan	11.45	1.02	0.681	7.96
400 nm	Reverse scan	10.02	1.03	0.509	5.25 (4.81 ± 0.17)
	Forward scan	10.01	1.02	0.556	5.68

[a] The devices were fabricated using compact ALD-TiO_2 HBL materials of varied thickness prepared *via* ALD. [b] The average values shown in parentheses were obtained from 15 devices fabricated under the same experimental conditions for each thickness.

surface of FTO. After that, the crystal grains were propagated and the film roughness increased. After the roughness reached the maximum at the film thickness of 200 nm, the filling of the rugged surface with TiO_2 nanoparticles in another layer is supposed to decrease the surface roughness. Although the rough surface is reported to affect the scattering and transmittance between HBL and PSK,[41] the results of finite-difference time-domain (FDTD) simulation indicate that the difference of R_{rms} from 10 to 40 nm scarcely affects the absorption, as shown in Fig. S3.†

The crystal structures of ALD-TiO_2, $MAPbI_3$ and $MAPbI_3$ on ALD-TiO_2 of thickness 200 nm were verified with X-ray diffraction (XRD) analysis on the FTO substrate (as shown in Fig. S4a†). The signals obtained for TiO_2 marked "*" confirm the formation of the anatase phase. Fig. S4† also shows the XRD investigations of $MAPbI_3$ films deposited on FTO and on ALD-TiO_2. The XRD signals of $MAPbI_3$ films were recorded to confirm the PSK tetragonal phase, pointing to the fully formed PSK structure from CH_3NH_3I and PbI_2.[42] No impurity signals were detected, indicating that the grown $MAPbI_3$ crystal structures were highly pure and adequately crystalline.

Analysis of the bare FTO and FTO covered with ALD-TiO_2 (200 nm) with a FESEM is shown in Fig. S4b and c.† The satisfactory homogeneity with a small grain structure enhanced the surface area of the under-layer and improved the net efficiency of the cells. The top image of $MAPbI_3$ on the ALD-TiO_2 layer was obtained using a FESEM as shown in Fig. S4d.† The PSK films were produced with the anti-solvent deposition technique with the addition of chlorobenzene through rapid-deposition crystallization (RDC), showing homogeneous morphology with large grains. For further confirmation of the formed PSK layer, we investigated the surface roughness using an AFM. R_{rms} of the $MAPbI_3$ film on ALD-TiO_2 was ~17.9 nm; the AFM images confirm the homogeneity and the large grain boundaries of the obtained film as shown in Fig. S4e.† For additional confirmation of the formation of the ALD-TiO_2 HBL and $MAPbI_3$, X-ray photoelectron spectra, both wide and narrow, for $MAPbI_3$ and $MAPbI_3$ on TiO_2 films yielded results shown in Fig. S5a–d.† Narrow X-ray photoelectron spectra of Ti $2p_{1/2}$ and Ti $2p_{3/2}$ for TiO_2 and O 1s for O_2, and narrow X-ray photoelectron spectra of Pb 4f and I 3d for $MAPbI_3$ and $MAPbI_3$ on TiO_2 were recorded. As expected, the sample displayed signals of carbon, nitrogen, iodine and lead, which were confirmed with the core-level intensity, indicating a slight deviation from the stoichiometry of $CH_3NH_3PbI_3$. We obtained the areas of the X-ray photoelectron spectra of these elements by fitting Gaussian peaks after removing the secondary-electron background, followed by normalization with the corresponding atomic sensitivity factors. The small proportions of nitrogen, carbon, lead and iodine can perhaps be attributed to the deficiency of CH_3NH_3I and PbI_2.[43] The binding energies for Pb 4f and with I 3d core levels agreed with Lindblad's results.[44] A singlet of the I $3d_{5/2}$ core level at binding energy 619.5 eV for both $TiO_2/CH_3NH_3PbI_3$ and FTO/$CH_3NH_3PbI_3$ samples with spin–orbit splitting 11.5 eV to the I $3d_{3/2}$ level was recorded for all samples. The distance of the binding energy between the Pb 4f and the I 3d core planes was equal in all samples.[45]

The charge-extraction properties were investigated for the as-fabricated PSC devices, based on ALD-TiO_2 as compact HBL films using the TCSPC technique for PSK deposited on ALD-TiO_2 films of varied thickness. We first measured steady-state PL to assess the effect of PL quenching of PSK due to the varied thickness of the ALD-TiO_2 films. As the PL spectra show in Fig. 5a, the PL intensities of PSK decreased significantly when the PSK layer was in contact with the ALD-TiO_2 compact layer of varied thickness. The PL intensities exhibited the order 400 nm > 300 nm > 10 nm > 50 nm > 100 nm > 200 nm, indicating an electron-extracting ability in the reverse order, *i.e.*, the 200 nm ALD-TiO_2 film had the best electron-extracting ability because of the existence of an efficient non-radiative process to quench the PL effectively. To further investigate the kinetics of this efficient non-radiative process, we measured transient PL decays using the TCSPC technique with excitation at 635 nm and probe at 770 nm. The PL transient profiles shown in Fig. 5b are well fitted with a tri-exponential decay function; the fitted time coefficients (τ_i) for each sample are shown in Table 2 with the corresponding relative amplitudes (A_i) shown in parentheses. The average PL lifetimes (τ_{PL}) were determined with an intensity-averaged approach reported elsewhere.[46] τ_{PL} for only $MAPbI_3$ deposited on FTO was determined to be 136 ns, but decreased to 67, 31, 31, 26, 74 and 85 ns when PSK was in contact with the ALD-TiO_2 compact layer of thickness 10, 50, 100, 200, 300 and 400 nm, respectively. If we suppose that electron extraction by the ALD-TiO_2 compact layer is the predominant path of non-radiative relaxation, the rates of interfacial electron transfer ($1/\tau_e$) in the $MAPbI_3$/ALD-TiO_2 interface are estimated to be 7.6×10^6, 2.5×10^7, 2.5×10^7, 3.1×10^7, 6.2×10^6 and 4.4×10^6 s^{-1} for thicknesses 10, 50, 100, 200, 300 and 400 nm of the ALD-TiO_2 compact layer, respectively; details of the determination of τ_{PL} and τ_e are summarized in Table 2. We found that the rate of electron transfer increased with increased thickness of the ALD-TiO_2 film until 200 nm but decreased significantly for a film thickness greater than 200 nm.

The rough surface might have increased the rate of electron transfer because of the increment of the interfacial area, because a satisfactory relationship between R_{rms} and $1/\tau_e$ was

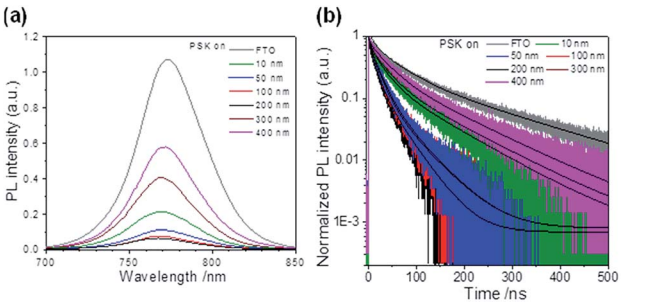

Fig. 5 (a) PL spectra and (b) PL decay profiles of PSK, and PSK deposited on varied compact ALD-TiO_2 HBL films. The PL spectra were obtained at excitation wavelength 633 nm; the transient PL decays were obtained using TCSPC with excitation at 635 nm and probe at 770 nm. The fitted results are represented in black lines for all results.

Table 2 Lifetimes (relative amplitudes) of compact ALD-TiO_2 HBL-based PSCs of varied thickness, with excitation at 635 nm, probe at 770 nm

Films	τ_1/ns (A_1)	τ_2/ns (A_2)	τ_3/ns (A_3)	τ_{PL}[a]/ns	$1/\tau_e$[b]/10^6 s^{-1}
PSK	11.7 (0.25)	51 (0.49)	187 (0.26)	135.9	—
PSK/10 nm ALD-TiO_2	6.2 (0.26)	26.0 (0.52)	97.5 (0.22)	67.0	7.6
PSK/50 nm ALD-TiO_2	4.8 (0.20)	18.3 (0.64)	51.5 (0.16)	30.8	25
PSK/100 nm ALD-TiO_2	4.3 (0.20)	17.5 (0.65)	52.5 (0.15)	30.6	25
PSK/200 nm ALD-TiO_2	1.5 (0.18)	12.8 (0.60)	38.3 (0.22)	25.7	31
PSK/300 nm ALD-TiO_2	5.5 (0.28)	30.0 (0.50)	107 (0.22)	74.3	6.2
PSK/400 nm ALD-TiO_2	4.0 (0.18)	33.5 (0.54)	116 (0.28)	85.3	4.4

[a] The average PL lifetimes were determined according to the following equation, $\tau_{PL} = \frac{\sum A_i \tau_i^2}{\sum A_i \tau_i}$ in which τ_i and A_i are the fitted time coefficients and the corresponding amplitudes of each component, respectively. [b] The interfacial hole-extraction time (τ_e) at the interface between PSK and HBL was predicted with this equation, $\frac{1}{\tau_e} = \frac{1}{\tau_{PSK/HBL}} - \frac{1}{\tau_{PSK}}$ in which τ_{PSK} and $\tau_{PSK/HBL}$ are the PL lifetimes for PSK only and those with PSK deposited on varied compact ALD-TiO_2 HBL films, respectively.

observed. Also, because the conductivity of TiO_2 might be a problem for a thicker film, we speculate that this anomalous phenomenon might be due to the effect of charge accumulation in the ALD-TiO_2/PSK interface that inhibits the interfacial electron transfer on the surface of ALD-TiO_2 with film thicknesses 300 and 400 nm. To confirm the relationship between the PL lifetimes of an ALD-TiO_2 compact layer, conductivities, and the effect on the device performances, we measured the resistivity of each ALD-TiO_2 compact layer with an electrochemical analyzer (ALS/CH Instruments 852C, ALS) and a copper lead wire. The resistivities were measured to be 235, 162, 67, 46, 324 and 1235 Ω cm for thicknesses 10, 50, 100, 200, 300 and 400 nm of the ALD-TiO_2 compact layer, respectively; the corresponding conductivities were estimated to be 4.23, 6.17, 14.9, 21.7, 3.09 and 0.81 mS m^{-1}, respectively. Fig. 6 shows a correlation of the PCE with the thickness of the ALD-TiO_2 compact layer with respect to the interfacial electron-transfer intervals and the conductivities. The best result was obtained from the sample of ALD-TiO_2 with film thickness 200 nm. These results are consistent with the photovoltaic performance in which the ALD-TiO_2 device of thickness 200 nm showed the greatest PCE, 15.0%.

ALD is a controllable method to prepare a compact layer with satisfactory reproducibility.[47] To assess the reproducibility of the cells, we fabricated 15 devices under the same experimental conditions for each ALD-TiO_2 thickness; the corresponding photovoltaic parameters of all devices with averages and standard deviations are summarized in Tables S1–S6.† Fig. 7a shows a histogram to compare the performance distributions of these results with the thickness of ALD-TiO_2 films, giving average PCE/% = 9.33 ± 0.14, 9.76 ± 0.33, 12.78 ± 0.19, 14.37 ± 0.44, 7.68 ± 0.23 and 4.81 ± 0.17 for devices made from ALD-TiO_2 of thickness 10, 50, 100, 200, 300 and 400 nm, respectively; the histograms for other photovoltaic parameters J_{sc}, V_{oc} and FF are shown in Fig. S6a–c.† Beyond the efficiency and reproducibility, stability is another important factor for PSC; we thus tested the stability of the ALD-TiO_2-based devices. The devices were stored in ambient air (humidity ~50% and temperature ~25 °C) and dark conditions to test the stability. As shown in Fig. 7b, the devices demonstrated satisfactory stability over a period of ~500 h. The results indicate that the efficiency of each device remained stable and maintained ~96% of its initial value until 200 h and then the efficiency decreased substantially to ~50% after storage for 500 h.

The photovoltaic performance of a PSC is related to many factors, such as film morphology, surface roughness, carrier

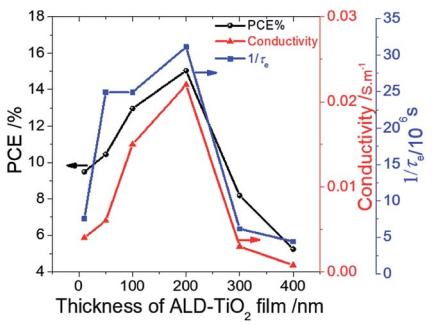

Fig. 6 Correlation of device performance (PCE/%) (black) with the thickness of an ALD-TiO_2 film with respect to conductivity/S m^{-1} (red) and rate of interfacial electron transfer ($1/\tau_e$/s^{-1}) (blue).

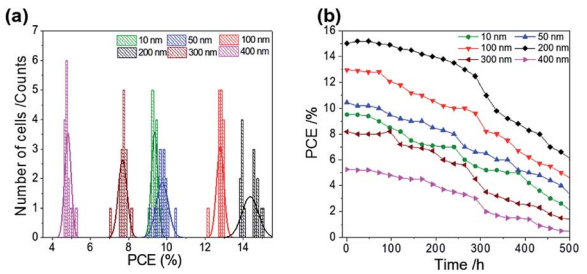

Fig. 7 (a) PCE distribution histogram; (b) PCE evolution of 15 devices stored in ambient air for varied duration/h for ALD-TiO_2 of thickness 10, 50, 100, 200, 300 and 400 nm, respectively, as a compact HBL.

lifetime and charge-transport properties. Using ALD-TiO_2 as HBL is an effective strategy to have the above-mentioned characteristics under sufficient control, which is critical to achieve high performance comparable with that of other HBLs studied elsewhere.[48]

Conclusions

We demonstrated that the morphology and thickness of the ALD-TiO_2 film as a compact layer play a crucial role in attaining a satisfactory device performance and decreased hysteresis for PSC with a n-i-p configuration. The compact layer designed by ALD is dense, uniform and homogeneous, which ensures only minor defects and maximum contact areas at the interfaces with the PSK/TiO_2 layers; it thus enhances charge separation at the PSK/TiO_2 interface and promotes electron transport through the ALD-TiO_2 layer. We investigated the photovoltaic performance of PSC devices made of an ALD-TiO_2 compact layer of film thicknesses varied in the range from 10 to 400 nm. The morphology and surface roughness of the ALD-TiO_2 films were investigated with a SEM and an AFM; the electron-transfer characteristics were investigated *via* steady-state PL and transient PL (*via* TCSPC) spectra. We found a systematic correlation between the device performance and the surface roughness and the conductivity of an ALD-TiO_2 film and the rate of electron transfer as a function of the thickness of an ALD-TiO_2 film; the best device performance attained PCE 15.0% at thickness 200 nm, at which great surface roughness and rapid electron transfer occurred. The ALD-TiO_2-based PSC devices also showed a minor effect of hysteresis with excellent reproducibility and satisfactory stability during storage in air. This work thus provides another alternative to fabricate mesoscopic PSCs using ALD to prepare a well-controlled TiO_2 compact layer of a desired thickness.

Experimental methods

Preparation of PSK precursor solution

Methyl ammonium iodide (CH_3NH_3I) was synthesized *via* the reaction of methylamine (CH_3NH_2, 21.6 mL, 40 mass% in water, Alfa Aesar) and hydroiodic acid (HI, 30 mL, 57 mass% in water, with hypophosphorous acid H_3PO_2 1.5%, Alfa Aesar) and stirred at 0 °C for 2 h under a N_2 atmosphere, followed by rotary evaporation to remove the solvent. The CH_3NH_3I powder was washed three times with diethyl ether (99%, anhydrous, ECHO) and dried in a vacuum oven at 50 °C overnight before use. CH_3NH_3I was synthesized as described elsewhere.[49–51] $MAPbI_3$ precursor solutions (concentration 45% by mass) were prepared in *N*,*N*-dimethyl formamide (DMF, anhydrous, Aldrich, 1 mL) mixed with powdered CH_3NH_3I (175 mg) and PbI_2 (99%, Aldrich, 507 mg). The solution was stirred at 70 °C for 1 h before use.

Fabrication of electrodes and devices

Before ALD, FTO (TEC7, Hartford, USA) was partially removed from the substrate *via* etching with zinc powder and HCl (2 M) to produce the desired pattern. The patterned FTO substrates were cleaned with ultrasonication for 30 min in a mixture (acetone, soapy water and isopropyl alcohol (IPA), 1 : 1 : 1) and then washed with deionized water. Afterwards, the glass was dried with a N_2 blower. Dense thin films of titanium dioxide as HBL with varied thickness were deposited onto the FTO substrate using a commercial hot-wall flow-type ALD reactor (SUNALETM R series, Picosun, Finland). The deposition involved alternating exposure of $TiCl_4$ and deionized water vapor at process temperature 300 °C with a precursor carrier and purge gas N_2 at pressure 1.6 kPa. The pulse and purge times for the precursors were 0.1 and 4 s, respectively. The rate of deposition of TiO_2 on the FTO glass was estimated to be 0.43 Å per cycle. To fabricate uniform, one-side deposited TiO_2 films, we attached the FTO glass tightly to a smooth cover glass, which was previously washed with deionized water in an ultrasonic bath for 5 min. After that, a m-TiO_2 layer of thickness approximately 200 nm was spin-coated (100 μL, 3000 rpm, 30 s) and annealed at 450 °C for 30 min. The substrates were subsequently exposed to ozone for 18 min *via* irradiation (excimer lamp PC-01-H, N-Cobo Co.) under an O_2 atmosphere to remove the organic residues. The prepared $MAPbI_3$ precursor solution was deposited onto the prepared substrate with spin coating at 5000 rpm for 15 s; a few drops of chlorobenzene (CBZ) as an anti-solvent were dripped onto the substrate during spin coating after a delay (5 s). The $MAPbI_3$-precursor coated substrates were then dried on a hot plate at 100 °C for 10 min. The HTM layer with a solution containing spiro-OMeTAD (125 mg, Lumtec), Li-TFSI (7.8 mg, Aldrich) in acetonitrile (15.6 μL) and 4-*tert*-butylpyridine (TBP, 22.6 μL) dissolved in chlorobenzene (1 mL) was then deposited *via* spin coating at 2000 rpm for 30 s. The sample was transferred to a vacuum system (10^{-6} Torr) in which silver (thickness ~ 150 nm) was evaporated through a shadow mask to complete the device fabrication; the active area of the Ag electrodes in the fabricated device was 0.09 cm^2.

Characterization of materials and devices

Structure and surface measurements. The crystalline phases were identified with XRD (RINT-2000/PC RIGAKU, Cu K_α radiation, scanning speed 2° (2θ)/min within 2θ range 5–60°). The particle morphology and structure were examined with a FESEM (Hitachi SU8010, maximum resolution 1 nm at electron acceleration voltage 15 kV) and an AFM (nanoscale hybrid microscope VN-8010, Keyence microscope, Japan). To analyze the chemical composition of the surfaces we used an X-ray photoemission spectrometer (JPS-9200, JEOL) to record the X-ray photoemission spectrum. The Al K_α line served as the X-ray source; the C 1s signal served as an internal reference (284.6 eV).

Photovoltaic and PL lifetime measurements. The *J*–*V* curves were measured with a digital source meter (Keithley 2400) under one-sun illumination (AM 1.5 G, 100 mW cm^{-2}) from a solar simulator (XES-40S1, SAN-E1). The IPCE spectra were recorded with a system comprising a Xe lamp (A-1010, PTi, 150 W) and monochromator (PTi, 1200 groove mm^{-1} blazed at 500

nm). PL transients were recorded with a TCSPC system (Fluotime200, PicoQuant) with excitation at 635 nm from a picosecond pulsed-diode laser (LDH-635, PicoQuant, FWHM $\sim$ 70 ps); the PL temporal profiles were recorded at 770 nm.

Conductivity measurements. We used an electrochemical analyzer (ALS/CH Instruments 852C, ALS) with a copper lead wire. The experimental setup of the measurements is as follows: two electrodes of the electrochemical analyzer were connected to the samples, one to the FTO part and the other to the compact ALD-TiO_2 surface. We measured the resistivity at various positions on the compact ALD-TiO_2 surface. Almost 15 positions have been tested for each sample to derive their mean. The distance between the two electrodes was stable for all measurements and for all compact ALD-TiO_2 of varied thickness to make the comparison among them more precise.

Numerical simulations. The FDTD simulation was performed with the Lumerical FDTD solution software package on a discrete, non-uniformly spaced mesh with a maximum resolution of 2.0 nm. The TiO_2 substrate was assumed to behave as a dielectric with a refractive index $n = 2.5$. In the simulation, a linear polarized plane wave was irradiated onto the structures from TiO_2 at a normal incidence angle; the surface roughness of TiO_2 at the interface of TiO_2 and PSK was varied from 0 to 40 nm as the root-mean-square roughness (R_{rms}).

Acknowledgements

We thank Mr Hau-Shiang Shiu for his assistance in SEM measurements. KAKENHI grant No. JP23225006, JP15H00856, JP15K17438, JP15H01073, JP15K04589, JP17H01041, and JP15K20833, Nanotechnology Platform (Hokkaido University) and Dynamic Alliance for Open Innovation Bridging Human, Environment and Materials (Five-Star Alliance) of MEXT, Taiwan Ministry of Science and Technology (contracts MOST 105-2119-M-009-011-MY3 and MOST 104-2119-M-009-001) supported this research. AES thanks National Chiao Tung University (Hsinchu, Taiwan) and Hokkaido University (Sapporo, Japan) for support of his visit to NCTU through the Elite Internship Program agreement between the two universities.

References

1 A. Kojima, K. Teshima, Y. Shirai and T. Miyasaka, *J. Am. Chem. Soc.*, 2009, **131**, 6050–6051.
2 M. M. Lee, J. Teuscher, T. Miyasaka, T. N. Murakami and H. J. Snaith, *Science*, 2012, **338**, 643–647.
3 W. S. Yang, J. H. Noh, N. J. Jeon, Y. C. Kim, S. Ryu, J. Seo and S. I. Seok, *Science*, 2015, **348**, 1234–1237.
4 Y. Zhao and K. Zhu, *J. Phys. Chem. Lett.*, 2014, **5**, 4175–4186.
5 J. Xiao, J. J. Shi, D. M. Li and Q. B. Meng, *Sci. China: Chem.*, 2015, **58**, 221–238.
6 S. D. Stranks, G. E. Eperon, G. Giulia, C. Menelaou, M. J. P. Alcocer, T. Leijtens, L. M. Herz, A. Petrozza and H. J. Snaith, *Science*, 2013, **342**, 341–344.
7 L. Etgar, P. Gao, Z. Xue, Q. Peng, A. K. Chandiran, B. Liu, M. K. Nazeeruddin and M. Grätzel, *J. Am. Chem. Soc.*, 2012, **134**, 17396–17399.
8 J. Wei, Y. Zhao, H. Li, G. Li, J. Pan, D. Xu, Q. Zhao and D. Yu, *J. Phys. Chem. Lett.*, 2014, **5**, 3937–3945.
9 J. M. Frost, K. T. Butler and A. Walsh, *APL Mater.*, 2014, **2**, 081506.
10 H.-W. Chen, N. Sakai, M. Ikegami and T. Miyasaka, *J. Phys. Chem. Lett.*, 2015, **6**, 164–169.
11 Y. Zhao, C. Liang, H. Zhang, D. Li, D. Tian, G. Li, X. Jing, W. Zhang, W. Xiao, Q. Liu, F. Zhang and Z. He, *Energy Environ. Sci.*, 2015, **8**, 1256–1260.
12 S. van Reenen, H. J. Snaith and M. Kemerink, *J. Phys. Chem. Lett.*, 2015, **6**, 3808–3814.
13 J. J. Shi, X. Xu, H. Y. Zhang, Y. H. Luo, D. M. Li and Q. B. Meng, *Appl. Phys. Lett.*, 2015, **107**, 163901.
14 H. Yu, H. Lu, F. Xie, S. Zhou and N. Zhao, *Adv. Funct. Mater.*, 2016, **26**, 1411–1419.
15 J. M. Azpiroz, E. Mosconi, J. Bisquert and F. De Angelis, *Energy Environ. Sci.*, 2015, **8**, 2118–2127.
16 E. L. Unger, E. T. Hoke, C. D. Bailie, W. H. Nguyen, A. R. Bowring, T. Heumuller, M. G. Christoforo and M. D. McGehee, *Energy Environ. Sci.*, 2014, **7**, 3690–3698.
17 O. Almora, C. Aranda, I. Zarazua, A. Guerrero and G. G. Belmonte, *ACS Energy Lett.*, 2016, **1**, 209–215.
18 W. Ke, G. Fang, H. Lei, P. Qin, H. Tao, W. Zeng, J. Wang and X. Zhao, *J. Power Sources*, 2014, **248**, 809–815.
19 P. J. Cameron and L. M. Peter, *J. Phys. Chem. B*, 2003, **107**, 14394–14400.
20 L. Kavan, N. Tetreault, T. Moehl and M. Grätzel, *J. Phys. Chem. C*, 2014, **118**, 16408–16418.
21 L. Kavan, B. O'Regan, A. Kay and M. Grätzel, *J. Electroanal. Chem.*, 1993, **346**, 291–307.
22 J. Xia, N. Masaki, K. Jiang and S. Yanagida, *J. Phys. Chem. B*, 2006, **110**, 25222–25228.
23 W. Ke, G. Fang, J. Wang, P. Qin, H. Tao, H. Lei, Q. Liu, X. Dai and X. Zhao, *ACS Appl. Mater. Interfaces*, 2014, **6**, 15959–15965.
24 B. Conings, L. Baeten, T. Jacobs, R. Dera, J. D'Haen, J. Manca and H. G. Boyen, *APL Mater.*, 2014, **2**, 081505.
25 A. K. Chandiran, A. Yella, M. T. Mayer, P. Gao, M. K. Nazeeruddin and M. Grätzel, *Adv. Mater.*, 2014, **26**, 4309–4312.
26 S. Chavhan, O. Miguel, H. J. Grande, V. Gonzalez-Pedro, R. S. Sanchez, E. M. Barea, I. Mora-Sero and R. Tena-Zaera, *J. Mater. Chem. A*, 2014, **2**, 12754–12760.
27 S. M. George, *Chem. Rev.*, 2009, **110**, 111–131.
28 X. Shi, K. Ueno, T. Oshikiri and H. Misawa, *J. Phys. Chem. C*, 2013, **117**, 24733–24739.
29 K. Nakamura, T. Oshikiri, K. Ueno, Y. Wang, Y. Kamata, Y. Kotake and H. Misawa, *J. Phys. Chem. Lett.*, 2016, **7**, 1004–1009.
30 Y. Wu, X. Yang, H. Chen, K. Zhang, C. Qin, J. Liu, W. Peng, A. Islam, E. Bi, F. Ye, M. Yin, P. Zheng and L. Han, *Appl. Phys. Express*, 2014, **7**, 052301.
31 A. Gao, S. Yang, L. Lei, S. Zhang, Q. Cao, J. Xie, J. Li and Y. Liu, *Chem. Lett.*, 2015, **44**, 624–626.
32 L. Chen, J. R. Wang, L. Q. Xie, C. Zhan, Z. Qin, J. Z. Zhou, J. W. Yan, B. W. Mao and Z. Q. Tian, *Electrochem. Commun.*, 2016, **68**, 40–44.

33 A. R. b. M. Yusoff and M. K. Nazeeruddin, *J. Phys. Chem. Lett.*, 2016, **7**, 851–866.
34 J. H. Heo, H. J. Han, D. Kim, T. K. Ahn and S. H. Im, *Energy Environ. Sci.*, 2015, **8**, 1602–1608.
35 X. Xu, H. Zhang, J. Shi, J. Dong, Y. Luo, D. Li and Q. Meng, *J. Mater. Chem. A*, 2015, **3**, 19288–19293.
36 M. Xiao, F. Huang, W. Huang, Y. Dkhissi, Y. Zhu, J. Etheridge, A. Gray-Weale, U. Bach, Y.-B. Cheng and L. Spiccia, *Angew. Chem., Int. Ed.*, 2014, **53**, 9898–9903.
37 B. Chen, X. J. Zheng, M. J. Yang, Y. Zhou, S. Kundu, J. Shi, K. Zhu and S. Priya, *Nano Energy*, 2015, **13**, 582–591.
38 H.-S. Kim, I.-H. Jang, N. Ahn, M. Choi, A. Guerrero, J. Bisquert and N.-G. Park, *J. Phys. Chem. Lett.*, 2015, **6**, 4633–4639.
39 B. Chen, M. Yang, S. Priya and K. Zhu, *J. Phys. Chem. Lett.*, 2016, **7**, 905–917.
40 O. Malinkiewicz, C. Roldan-Carmona, A. Soriano, E. Bandiello, L. Camacho, M. K. Nazeeruddin and H. J. Bolink, *Adv. Energy Mater.*, 2014, **4**, 1400345.
41 H. Hu, B. Dong, H. Hu, F. Chen, M. Kong, Q. Zhang, T. Luo, L. Zhao, Z. Guo, J. Li, Z. Xu, S. Wang, D. Eder and L. Wan, *ACS Appl. Mater. Interfaces*, 2016, **8**, 17999–18007.
42 K. Liang, D. B. Mitzi and M. T. Prikas, *Chem. Mater.*, 1998, **10**, 403–411.
43 X. Liu, C. Wang, L. Lyu, C. Wang, Z. Xiao, C. Bi, J. Huang and Y. Gao, *Phys. Chem. Chem. Phys.*, 2015, **17**, 896–902.
44 R. Lindblad, D. Bi, B. Park, J. Oscarsson, M. Gorgoi, H. Siegbahn, M. Odelius, E. M. J. Johansson and H. Rensmo, *J. Phys. Chem. Lett.*, 2014, **5**, 648–653.
45 N. J. Jeon, J. H. Noh, Y. C. Kim, W. S. Yang, S. Ryu and S. I. Seok, *Nat. Mater.*, 2014, **13**, 897–903.
46 B. Valeur, in *Encyclopedia of Applied Physics*, Wiley-Vch, 2009.
47 L. Chen, J.-R. Wang, L.-Q. Xie, C. Zhan, Z. Qiu, J.-Z. Zhou, J.-W. Yan, B.-W. Mao and Z.-Q. Tian, *Electrochem. Commun.*, 2016, **68**, 40–44.
48 S. Duenas, H. Castan, H. Garcia, E. San Andres, M. Toledano-Luque, I. Martil, G. Gonzalez-Diaz, K. Kukli, T. Uustare and J. Aarik, *Semicond. Sci. Technol.*, 2005, **20**, 1044–1051.
49 K. C. Wang, J. Y. Jeng, P. S. Shen, Y. C. Chang, E. W. Diau, C. H. Tsai, T. Y. Chao, H. C. Hsu, P. Y. Lin, P. Chen, T. F. Guo and T. C. Wen, *Sci. Rep.*, 2014, **4**, 4756.
50 C.-Y. Chan, Y. Wang, G.-W. Wu and E. W.-G. Diau, *J. Mater. Chem. A*, 2016, **4**, 3872–3878.
51 C.-C. Chung, C. S. Lee, E. Jokar, J. H. Kim and E. W.-G. Diau, *J. Phys. Chem. C*, 2016, **120**, 9619–9627.